PAPER

Effect of porphyrin ligands on the catalytic CH₄ oxidation activity of monocationic μ-nitrido-bridged iron porphyrinoid dimers by using H₂O₂ as an oxidant†

Yasuyuki Yamada, [ID] *[a,b] Yusuke Miwa,[a] Yuka Toyoda,[b] Yoshiki Uno,[a] Quan Manh Phung [ID] [a,c] and Kentaro Tanaka [ID] *[a]

The μ-nitrido-bridged iron phthalocyanine homodimer is a potent molecule-based CH₄ oxidation catalyst that can effectively oxidize chemically stable CH₄ under mild reaction conditions in an acidic aqueous solution including an oxidant such as H₂O₂. The reactive intermediate is a high-valent iron-oxo species generated upon reaction with H₂O₂. However, a detailed comparison of the CH₄ oxidation activity of the μ-nitrido-bridged iron phthalocyanine dimer with those of μ-nitrido-bridged iron porphyrinoid dimers containing one or two porphyrin ring(s) has not been yet reported, although porphyrins are the most important class of porphyrinoids. Herein, we compare the catalytic CH₄ and CH₃CH₃ oxidation activities of a monocationic μ-nitrido-bridged iron porphyrin homodimer and a monocationic μ-nitrido-bridged heterodimer of an iron porphyrin and an iron phthalocyanine with those of a monocationic μ-nitrido-bridged iron phthalocyanine homodimer in an acidic aqueous solution containing H₂O₂ as an oxidant. It was demonstrated that the CH₄ oxidation activities of monocationic μ-nitrido-bridged iron porphyrinoid dimers containing porphyrin ring(s) were much lower than that of a monocationic μ-nitrido-bridged iron phthalocyanine homodimer. These findings suggested that the difference in the electronic structure of the porphyrinoid rings of monocationic μ-nitrido-bridged iron porphyrinoid dimers strongly affected their catalytic light alkane oxidation activities.

Introduction

Methane (CH₄) is a naturally abundant molecule commonly found in natural gas or as methane hydrate. Moreover, the Sabatier process enables the efficient conversion of CO₂ into CH₄ through a reaction with H₂ in the presence of a Ni catalyst. Therefore, CH₄ has long been regarded as a next-generation carbon resource for the production of industrially valuable chemical raw materials. However, CH₄ is well-recognized as a chemically stable compound with a particularly high C–H bond dissociation energy of 104.9 kcal mol⁻¹. This feature implies that achieving efficient low-temperature conversion into industrially useful organic molecules, such as MeOH, is highly challenging.[1,2] Therefore, significant efforts have been devoted to developing novel catalysts for the efficient low-temperature conversion of CH₄.

In nature, soluble methane monooxygenase (sMMO) is known to efficiently convert CH₄ into MeOH in an aqueous solution under ambient reaction conditions by utilizing a high-valent iron-oxo species as its catalytic intermediate.[3–5] This observation has stimulated the interest of chemists to investigate the mechanism at the sMMO reaction center and inspire the production of a large variety of biomimetic high-valent iron-oxo species. These studies successfully elucidated the reaction mechanism of sMMOs, revealing that the proton-coupled electron transfer (PCET) pathway facilitates the low-temperature and efficient oxidation of CH₄ by high-valent iron-oxo species.[6–10]

However, there is still a limited number of artificial molecular iron-oxo-based biomimetic catalysts that effectively activate the C–H bonds of CH₄ at temperatures below 100 °C.[5,11,12] This is most likely due to the high stability of CH₄. μ-Nitrido-bridged iron porphyrinoid dimers, such as μ-nitrido-bridged iron phthalocyanine homodimers **1** or **1**⁺ (Fig. 1a), are among

*a*Department of Chemistry, Graduate School of Science, Nagoya University, Furo-cho, Chikusa-ku, Nagoya 464-8602, Japan.
E-mail: Yamada.yasuyuki.i6@f.mail.nagoya-u.ac.jp, kentaro@chem.nagoya-u.ac.jp
*b*Research Center for Materials Science, Nagoya University, Furo-cho, Chikusa-ku, Nagoya 464-8602, Japan
*c*Institute of Transformaytive Bio-Molecules (ITBM), Nagoya University, Furo-cho, Chikusa-ku, Nagoya 464-8602, Japan
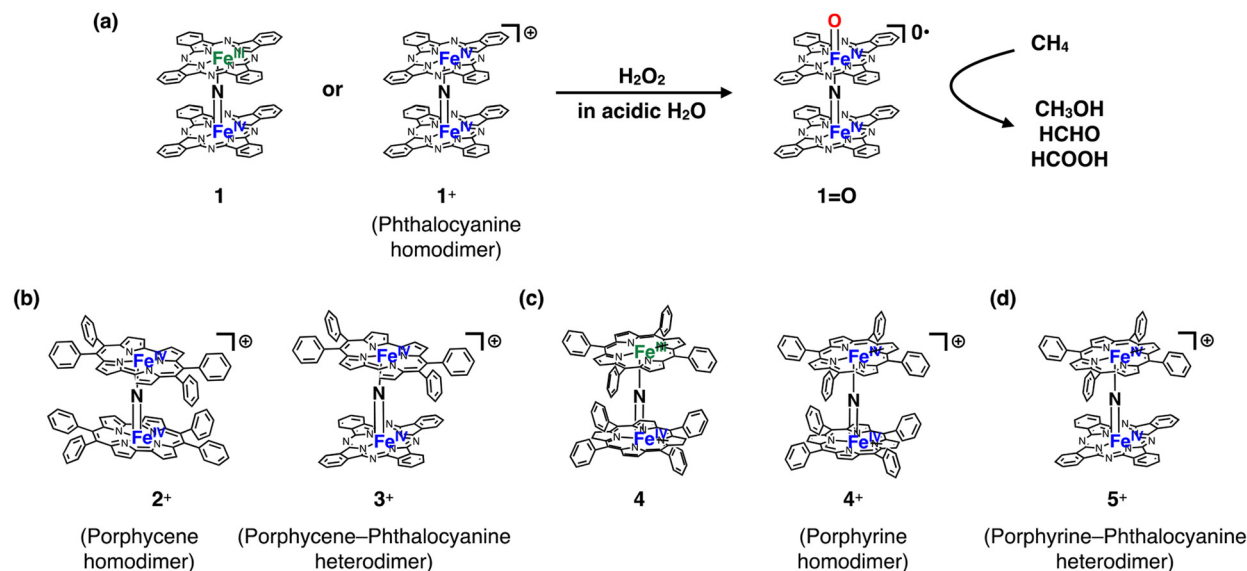
Fig. 1 (a) Formation of high-valent iron oxo species **1**═**O** with a potent CH_4 oxidation ability from a neutral (**1**) or monocationic (**1**$^+$) μ-nitrido-bridged iron phthalocyanine homodimer upon reaction with H_2O_2. (b) Structures of a monocationic μ-nitrido-bridged iron porphycene homodimer (**2**$^+$) and monocationic μ-nitrido-bridged heterodimer of an iron porphycene and an iron phthalocyanine (**3**$^+$). (c) Structures of a neutral μ-nitrido-bridged iron porphyrin homodimer (**4**) and monocationic μ-nitrido-bridged iron porphyrin homodimer (**4**$^+$). (d) Structure of a μ-nitrido-bridged heterodimer of an iron porphyrin and an iron phthalocyanine (**5**$^+$).

few iron-oxo-based molecular catalysts capable of actually activating the C–H bonds of CH_4 in acidic aqueous solutions containing H_2O_2 at a temperature lower than 100 °C.[11,13–17] The reactive intermediate of the CH_4 oxidation catalyzed by either **1** or **1**$^+$ is considered to be the high-valent iron-oxo species **1**═**O** generated *in situ* upon reaction with H_2O_2.[11,18] A DFT calculation study indicated the importance of the core μ-nitrido-bridged dinuclear iron structure (Fe–N═Fe) for the high CH_4 oxidation activity of **1**═**O**.[19] It has also been demonstrated that catalysts based on μ-nitrido-bridged iron porphyrinoid dimers are applicable to the oxidation of other stable organic chemicals such as benzene and ethane in aqueous media.[20–23]

On the other hand, we recently demonstrated that the introduction of porphycene ring(s), a well-known class of porphyrinoids, into a monocationic μ-nitrido-bridged iron porphyrinoid dimer [**2**$^+$ (μ-nitrido-bridged iron porphycene homodimer) or **3**$^+$ (μ-nitrido-bridged heterodimer of an iron phthalocyanine and an iron porphycene), Fig. 1b] dramatically changed the reactivity and decreased the stability of the corresponding high-valent iron-oxo species generated through the reaction with H_2O_2.[24,25] This suggests that the porphyrinoid structure is also an important factor in determining the reactivity of μ-nitrido-bridged iron porphyrinoid dimers.

Inspired by these previous studies, we became interested in the reactivity of porphyrin-containing μ-nitrido-bridged iron porphyrinoid dimers. Obviously, porphyrin is the representative pigment among the porphyrinoids. The synthesis of neutral μ-nitrido-bridged iron porphyrin homodimer **4** (Fig. 1c) was reported by Cohen *et al.* in 1976,[26] which is 8 years earlier than the first report on the synthesis of neutral phthalocyanine homodimer **1** by Ercolani *et al.*[27] Sorokin *et al.*

demonstrated that a high-valent iron-oxo species with a spin state of $S = 1/2$ was generated through the reaction of a neutral μ-nitrido-bridged iron porphyrin homodimer with *m*-chloroperbenzoic acid (*m*CPBA).[18] Although it was confirmed that a neutral form of μ-nitrido-bridged iron porphyrin homodimer **4** exhibited catalytic CH_4 oxidation activity in the presence of *m*CPBA,[18] no report exists directly comparing the reactivities of μ-nitrido-bridged iron porphyrin homodimers (**4** or **4**$^+$, Fig. 1c) and μ-nitrido-bridged heterodimers of an iron phthalocyanine and an iron porphyrin (**5** or **5**$^+$, Fig. 1d) with that of μ-nitrido-bridged iron phthalocyanine homodimers (**1** or **1**$^+$) under the same reaction conditions, despite the similar structure of porphyrin and phthalocyanine. Especially, the catalytic oxidation activities of μ-nitrido-bridged heterodimers of an iron phthalocyanine and an iron porphyrin (**5** or **5**$^+$) have not been described yet. Herein, we present a comparison of the catalytic CH_4 and CH_3CH_3 oxidation activities of a monocationic μ-nitrido-bridged iron porphyrin homodimer (**4**$^+$) and a monocationic μ-nitrido-bridged heterodimer of an iron porphyrin and an iron phthalocyanine (**5**$^+$) with those of a monocationic μ-nitrido-bridged iron phthalocyanine dimer (**1**$^+$) in an acidic aqueous solution containing H_2O_2 as oxidant.

Results and discussion

Synthesis of monocationic μ-nitrido-bridged iron porphyrinoid dimers containing porphyrin rings (**4**$^+$ and **5**$^+$)

The monocationic iron porphyrin dimer **4**$^+$ was synthesized by modifying the methods reported by the Suslick as well as our groups (Fig. 2a).[28,29] Iron tetraphenyl porphyrin chloride **6** was
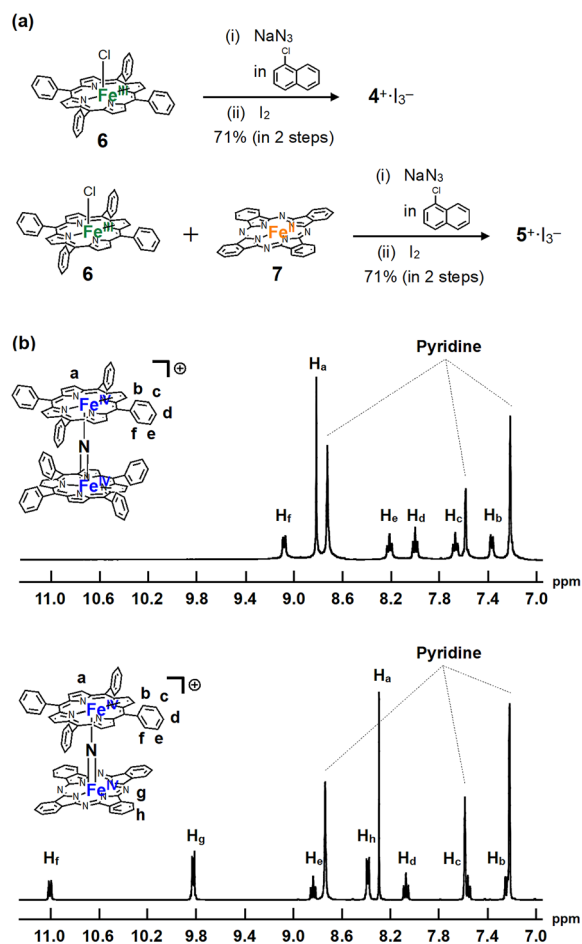
Fig. 2 (a) Synthesis of monocationic homodimer $4^+ \cdot I_3^-$ and heterodimer $5^+ \cdot I_3^-$. (b) ^{1}H-NMR spectra of $4^+ \cdot I_3^-$ and $5^+ \cdot I_3^-$ in pyridine-d_5.

heated with an excess of NaN_3 in 1-chloronaphthalene at 280 °C for 2 h to afford neutral μ-nitrido bridged iron porphyrin dimer **4**, which underwent subsequent oxidation by I_2 to give the desired monocationic species $4^+ \cdot I_3^-$. A monocationic μ-nitrido-bridged heterodimer of an iron porphyrin and an iron phthalocyanine was synthesized in a similar manner by heating a 1 : 1 mixture of iron porphyrin **6** and iron phthalocyanine **7** in 1-chloronaphthalene in the presence of an excess of NaN_3 at 280 °C for 2 h, followed by oxidation with I_2 to afford $5^+ \cdot I_3^-$ in a moderate yield (71%). Elemental analysis suggested that the counter anion of the monocationic heterodimer was triiodide, which was further confirmed by the results of single-crystal X-ray structural analysis (*vide infra*).

^{1}H-NMR and MALDI-TOF MS analyses were performed to characterize $4^+ \cdot I_3^-$ and $5^+ \cdot I_3^-$. In the MALDI-TOF MS spectra shown in Fig. S1 and S2 in the ESI,† signals corresponding to 4^+ and 5^+ were observed at around $m/z = 1350.3$ and $m/z = 1250.4$, respectively, which corresponded to the theoretical isotope distribution pattern of 4^+ and 5^+. As shown in Fig. 2b, all the ^{1}H-NMR peaks of both $4^+ \cdot I_3^-$ and $5^+ \cdot I_3^-$ were observed as sharp signals within the 7–11 ppm range, indicating that $4^+ \cdot I_3^-$ and $5^+ \cdot I_3^-$ include two Fe(IV) centers interacting with

each other in an antiferromagnetic fashion as in the case of other monocationic μ-nitrido-bridged iron porphyrinoid dimers (1^+, 2^+, or 3^+).[30,31] Furthermore, two sets of signals attributable to the *o*- and *m*-protons of the peripheral phenyl groups of tetraphenyl porphyrins (TPPs) were observed, suggesting that the rotation of the peripheral phenyl groups of TPPs was restricted due to the steric repulsion between the phenyl groups and porphyrin rings in both $4^+ \cdot I_3^-$ and $5^+ \cdot I_3^-$. On the other hand, the fact that the porphyrin and phthalocyanine rings of $4^+ \cdot I_3^-$ and $5^+ \cdot I_3^-$ were observed as C_2 symmetrical structures implies that the rotation of the TPP or phthalocyanine rings along the Fe–N≡Fe axis was sufficiently fast compared to the NMR timescale for both $4^+ \cdot I_3^-$ and $5^+ \cdot I_3^-$.

A comparison of the UV-Vis spectra of $4^+ \cdot PF_6^-$ and $5^+ \cdot PF_6^-$ with that of a monocationic μ-nitrido-bridged iron phthalocyanine homodimer $1^+ \cdot I^-$ in pyridine is shown in Fig. 3. Under these conditions, pyridine is expected to coordinate to the iron centers of $4^+ \cdot PF_6^-$, $5^+ \cdot PF_6^-$, and $1^+ \cdot I^-$. The bands at 425 nm of $5^+ \cdot PF_6^-$ were assignable to the Soret bands of porphyrin, which were slightly shifted to longer wavelengths compared to that of $4^+ \cdot PF_6^-$ (423 nm). More conspicuously, the Q-band of the phthalocyanine of $5^+ \cdot PF_6^-$ (740 nm) was shifted to a much longer wavelength compared to that of $1^+ \cdot I^-$ (636 nm). Single crystal X-ray structural analysis of $1^+ \cdot I^-$ demonstrated that the iodide anion (I^-) in $1^+ \cdot I^-$ was not coordinated to the iron center in a pyridine solution.[32] Considering that PF_6^- would not coordinate to the iron center of 5^+ in pyridine, which can coordinate more strongly than PF_6^-, it could be concluded that the electronic structure of both the iron porphyrin and iron phthalocyanine in $5^+ \cdot PF_6^-$ differed significantly from those in $4^+ \cdot PF_6^-$ and $1^+ \cdot I^-$ due to the pronounced electronic interaction between these two moieties.

Single crystal X-ray structural analysis

Dimers $4^+ \cdot I_3^-$ and $5^+ \cdot I_3^-$ were successfully crystallized in the triclinic space group ($P\bar{1}$) by slow evaporation of solvent from a mixture of $CHCl_3$ and pyridine. The molecular structures of $4^+ \cdot I_3^-$ and $5^+ \cdot I_3^-$ are shown in Fig. 4a–d. A comparison of some
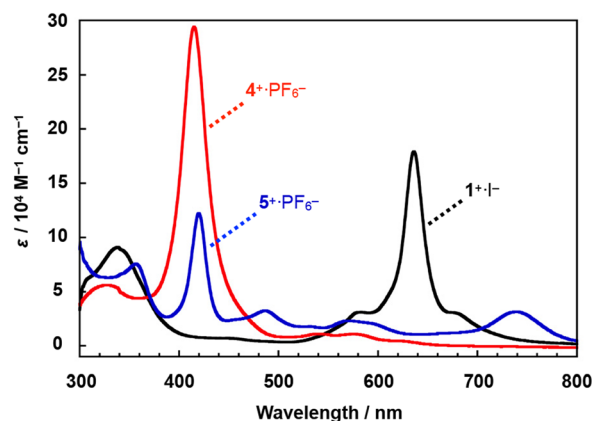
Fig. 3 (a) Comparison of the UV-Vis spectra of heterodimer $5^+ \cdot PF_6^-$ and homodimers $1^+ \cdot I^-$ and $4^+ \cdot PF_6^-$ in pyridine at 20 °C.
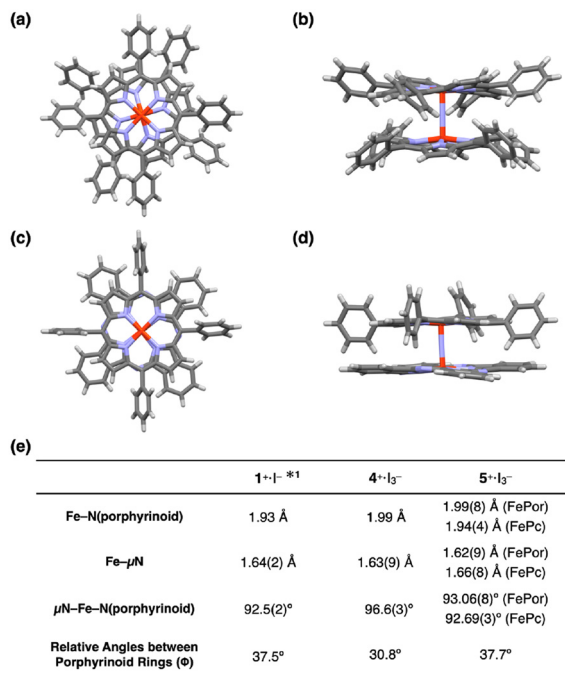
Fig. 4 (a) Top and (b) side views of the single crystal X-ray structure of $4^{+}\cdot I_3^{-}$. (c) Top and (d) side views of the single crystal X-ray structure of $5^{+}\cdot I_3^{-}$. I_3^{-}, coordinating pyridines, and crystalline solvents were omitted for clarity. (e) Comparison of some mean bond lengths and angles of $1^{+}\cdot I^{-}$, $4^{+}\cdot I_3^{-}$, and $5^{+}\cdot I_3^{-}$. *1: ref. 32.

structural parameters of $4^{+}\cdot I_3^{-}$ and $5^{+}\cdot I_3^{-}$ with the previously reported crystal structure of $1^{+}\cdot I^{-}$ is summarized in the table in Fig. 4e.

The porphyrin rings in the porphyrin homodimer $4^{+}\cdot I_3^{-}$ were significantly distorted from the flat π-plane (Fig. 4b), whereas no significant distortion was observed in the porphyrin rings of heterodimer $5^{+}\cdot I_3^{-}$. The observed porphyrin ring distortion was likely due to the steric repulsion of the peripheral phenyl rings in $4^{+}\cdot I_3^{-}$. In contrast, the peripheral phenyl rings of the iron tetraphenyl porphyrin of $5^{+}\cdot I_3^{-}$ located between the benzene rings of the iron phthalocyanine prevented steric repulsion. The mean bond distances between the four porphyrin nitrogen atoms and the coordinated Fe(IV) ion in $4^{+}\cdot I_3^{-}$ was 1.99 Å, which is almost identical to that between the four porphyrin nitrogens and the coordinated Fe(IV) ion in $5^{+}\cdot I_3^{-}$ [1.99(8) Å]. Similarly, the mean bond distances between the four phthalocyanine nitrogens and the coordinated Fe(IV) ion in $5^{+}\cdot I_3^{-}$ were almost identical to that in phthalocyanine homodimer $1^{+}\cdot I^{-}$ (1.93 Å). These differences in mean distances between the porphyrinoid nitrogens (Fe–N(porphyrinoid)) and their coordinated Fe(IV) ions reflected the fact that phthalocyanines generally possess narrower central cavities than porphyrins.

The average distance between the μ-nitrogen and iron ions of $4^{+}\cdot I_3^{-}$ was 1.64 Å, which is almost identical to that of $1^{+}\cdot I^{-}$. In both complexes, the μ-nitrogen is located almost in the center of the Fe–μN–Fe structures, suggesting the conjugation

of a single Fe–μN bond with a double Fe=μN bond in $4^{+}\cdot I_3^{-}$ and $1^{+}\cdot I^{-}$. The Fe–μN bond can be, therefore, assigned as 1.5 (*vide infra*, see DFT calculation section). In the case of $5^{+}\cdot I_3^{-}$, the distance between the μ-nitrogen and iron ion of the iron porphyrin (Fe(Por)–μN) was 1.62(9) Å, whereas the distance between the μ-nitrogen and iron ion of the iron phthalocyanine (Fe(Pc)–μN) was 1.66(8) Å. Considering the relatively large standard deviations of these values, it seems to be difficult to claim the difference from 1.64 Å. However, the fact that the Fe(Por)–μN was larger than the Fe(Pc)–μN might imply that, in $5^{+}\cdot I_3^{-}$, the Fe(Por)–μN has a higher double-bond (Fe=N) character, while the Fe(Pc)–μN has a higher single-bond (Fe–N) character. It should also be noted that a similar difference in the distance between μ-N and Fe ion was observed in a monocationic μ-nitrogen-bridged heterodimer of an iron(IV) phthalocyanine and iron(IV) porphycene.[25]

As for the average bond angles of the μ-nitrogen–Fe–nitrogens(porphyrinoid) (μN–Fe–N(porphyrinoid)), the value of $4^{+}\cdot I_3^{-}$ was slightly larger [96.6(3)°] than those in $1^{+}\cdot I^{-}$ and $5^{+}\cdot I_3^{-}$. This could be related to the structural distortion of the porphyrin ring in $4^{+}\cdot I_3^{-}$. The reason why the relative angle between the porphyrinoid rings in $4^{+}\cdot I_3^{-}$ (30.8°) was slightly smaller than those of $1^{+}\cdot I^{-}$ and $5^{+}\cdot I_3^{-}$ can be attributable to the steric repulsion of the peripheral phenyl rings and porphyrin core of $4^{+}\cdot I_3^{-}$.

Among a variety of μ-heteroatom-bridged iron porphyrinoid dimers, the structures of μ-oxo- or μ-hydroxo-bridged iron porphyrin dimers, where iron ions are generally in the 3+ states and the Fe–μO bondings have single-bond characters with slightly bent Fe–μO–Fe angles, are well-examined by single crystal X-ray structural analyses, allowing us to compare the structures with those of $4^{+}\cdot I_3^{-}$ and $5^{+}\cdot I_3^{-}$.[33] The Fe–N(porphyrin) distances of μ-oxo- or μ-hydroxo-bridged iron porphyrin dimers are approximately 2.08 Å, which are apparently longer than that in $4^{+}\cdot I_3^{-}$ and $5^{+}\cdot I_3^{-}$. These differences might be because of the differences in the oxidation states of the iron centers. The μ-oxo- or μ-hydroxo-bridged iron porphyrin dimers have the Fe–μO distances of 1.76–1.90 Å, which are apparently longer than those of the Fe–μN distances in $4^{+}\cdot I_3^{-}$ and $5^{+}\cdot I_3^{-}$. These results clearly indicate the double-bond character of the Fe–μN bondings in $4^{+}\cdot I_3^{-}$ and $5^{+}\cdot I_3^{-}$.

Cyclic voltammetry

The cyclic voltammograms of $1^{+}\cdot I^{-}$, $4^{+}\cdot PF_6^{-}$, and $5^{+}\cdot PF_6^{-}$ in pyridine solutions containing 100 mM $n\mathrm{Bu_4N^+ \cdot PF_6^-}$ were compared, as shown in Fig. 5. The cyclic voltammograms of a μ-nitrido-bridged iron phthalocyanine dimer and μ-nitrido-bridged iron porphyrin dimer have already been studied by the groups of Bottomley and Ercolani, and Kadish and Goff, respectively.[30,34] According to these previous reports, the four reversible 1e⁻ reductions of $1^{+}\cdot I^{-}$ at −0.58, −1.52, −1.74, and −2.00 V *vs.* Fc/Fc⁺ were assignable to the reduction of the iron centers, whereas the one irreversible oxidation wave at −0.19 V was due to that of the phthalocyanine ring. Similarly, the two reversible 1e⁻ reductions of $4^{+}\cdot PF_6^{-}$ at −0.82 and −1.69 V *vs.* Fc/Fc⁺ were attributable to the reduction of the iron centers,
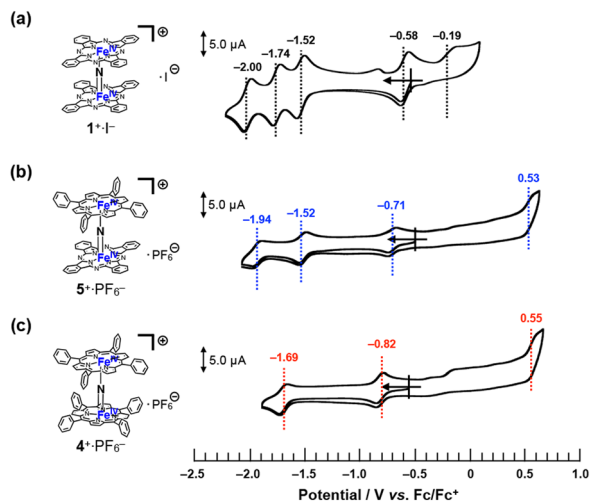
Fig. 5 Comparison of cyclic voltammograms of (a) $1^+ \cdot I^-$, (b) $5^+ \cdot PF_6^-$, and (c) $4^+ \cdot PF_6^-$ in a pyridine solution containing 100 mM of $^nBu_4N^+ \cdot PF_6^-$ at room temperature. [Substrate] = 200 μM, [scan rate] = 100 mV s^{-1}.

whereas the irreversible oxidation wave at 0.55 V was assignable to that of the porphyrin ring.

Based on these results, the three reversible 1e$^-$ reductions of $5^+ \cdot PF_6^-$ at −0.71, −1.52, and −1.94 V vs. Fc/Fc$^+$ were attributed to the reduction of the iron centers. As for the oxidation of $5^+ \cdot PF_6^-$ at 0.53 V, theoretical calculations suggested that the phthalocyanine ring was more easily oxidized than the porphyrin ring (vide infra, see "DFT calculations" section).

Overall, it could be concluded that the reduction potential assignable to Fe(IV)Fe(IV)/Fe(III)Fe(IV) of these monocationic μ-nitrido-bridged iron porphyrinoid dimers showed negative shift as the number of tetraphenylporphyrins increased (−0.58 V for $1^+ \cdot I^-$, −0.71 V for $5^+ \cdot PF_6^-$, and −0.82 V for $4^+ \cdot PF_6^-$), whereas the oxidation potential of the porphyrinoid ring was shifted to a higher potential (−0.19 V for $1^+ \cdot I^-$, 0.53 V for $5^+ \cdot PF_6^-$, and 0.55 V for $4^+ \cdot PF_6^-$). Thus, it was confirmed that the difference in the porphyrinoid structure significantly affected the electronic structure of the μ-nitrido-bridged iron porphyrinoid dimer.

ESI-TOF MS analysis of high-valent iron-oxo species

To confirm the generation of high-valent iron-oxo species, i.e., the reactive intermediates generated in the oxidation reaction upon treatment of either $4^+ \cdot I_3^-$ or $5^+ \cdot I_3^-$ with H$_2$O$_2$ in an aqueous solution, ESI-TOF MS measurements were performed on an acetonitrile solution of either $4^+ \cdot I_3^-$ or $5^+ \cdot I_3^-$ after addition of aqueous H$_2$O$_2$.

As shown in Fig. 6, the signals assignable to the high-valent iron-oxo species ($[4 + O]^+$ (see Fig. 6a) and $[5 + O]^+$ (see Fig. 6b)) were observed after addition of aqueous H$_2$O$_2$ at room temperature, and their isotopic distribution patterns corresponded to those calculated. In the case of $5^+ \cdot I_3^-$, the signals due to the hydroperoxo species $[5 + OOH + H]^+$ were clearly observed at around $m/z = 1284$. These results demonstrate that high-valent iron-oxo species were generated by treating either
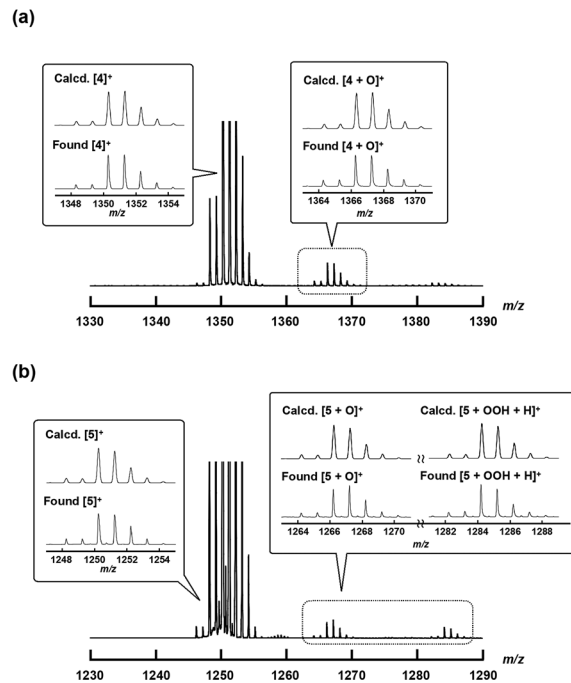

Fig. 6 ESI-TOF MS spectra of $4^+ \cdot I_3^-$ or $5^+ \cdot I_3^-$ in an aqueous CH$_3$CN solution containing an excess amount of H$_2$O$_2$ at room temperature (the detailed experimental procedure is shown in the Experimental section). Insets: Comparison of calculated (top) and experimental (bottom) isotopic distribution patterns of the molecular peaks assignable to $[4]^+$, $[4=O]^+$, $[5]^+$, $[5=O]^+$, and $[5 + OOH + H]^+$.

4^+ or 5^+ with H$_2$O$_2$ via the corresponding hydroperoxo species, as in the case of other μ-nitrido-bridged iron phthalocyanine dimers. However, in the case of the heterodimer of an iron porphyrin and iron phthalocyanine 5^+, it was difficult to determine the accurate position of the Fe=O moiety, i.e., whether it was located on the iron porphyrin or iron phthalocyanine group.[25]

DFT calculations

In order to better understand and explain the experimental data, we conducted density functional theory (DFT) calculations on **4**, **5**, and **1**. The computational details can be found in the Experimental section. Our primary focus was directed towards analyzing the redox processes involving these species (for example 4^+, 4^{2+}, and **4**). The electronic configurations of the monocationic complexes have been previously elucidated by Ghosh et al.[35] and Sorokin et al.,[11] and can be succinctly described as $(d_{xy})^2 (d_{xy})^2 (d_{xz} - d_{xz})^2 (d_{yz} - d_{yz})^2$. In agreement with the experimental data, the calculations revealed the symmetry of complexes 4^+ and 1^+. Specifically, we found that in 1^+, the Fe–N(Pc) and Fe–μN bond lengths were 1.953 and 1.590 Å, respectively. In 4^+, the corresponding bond distances were slightly longer, i.e., 1.986 and 1.601 Å. The Fe–N results confirmed the notion that the cavity of phthalocyanine is smaller than that of porphyrin. In all cases, Fe–N bond distances of less than 2.0 Å are compatible with the low-spin nature of the

Fe centers. In both 4^+ and 1^+, the Wiberg Fe–μN bond order is 1.61, with a contribution of around 0.8 from $Fe(d_{xz})$–$N(p_x)$ and $Fe(d_{yz})$–$N(p_y)$ π interactions (Table S12†). In 5^+, the two macrocycles caused a subtle distortion of the Fe–N–Fe axis. The Fe–μN bond distances were 1.587 and 1.600 Å. Although the DFT analysis suggested shorter bond distances than the experimental data (probably due to crystal packing), it correctly predicts a shorter bond distance between the Fe of iron porphyrin and μ-N, with a Wiberg bond order of 1.66. This bond exhibits a π character of around 0.90 from $Fe(d_{xz})$–$N(p_x)$ and $Fe(d_{yz})$–$N(p_y)$ interactions. The observed π character is slightly larger than that found in the bond between Fe of iron phthalocyanine and μN (0.76). Similar to what was observed in 4^+ and 1^+, the Fe–N(P) average bond distance (2.001 Å) was around 0.05 Å longer than the Fe–N(Pc) average bond distance (1.954 Å).

In analogy to our previous work,[25] the Fe–μN bonds became weaker upon reduction of 4^+, 1^+, and 5^+ due to the occupation of an antibonding orbital $Fe(d_{z^2}) - 2s + Fe(d_{z^2})$. The Fe–μN bond distances in the reduced complexes were systematically longer by 0.02 to 0.04 Å. Spin populations as well as spin density (Fig. 7) revealed that only the Fe–N–Fe axis was involved in the reduction. We found a major spin population on the Fe atoms, whereas the spin population of the macrocycles was small (less than 0.04). The two Fe centers were very similar, indicating that the oxidation state of iron in all reduced complexes could be formally assigned to 3.5. The reduction free energies, defined as the difference between the Gibbs free energies of the monocationic and neutral complexes $\Delta G_{red} = G_X - G_{X^+}$, were calculated. The reduction free energies of 1^+, 4^+, and 5^+ were computed as −5.1, −4.4, and −4.8 eV, respectively. The results were consistent with the cyclic voltammetry data, where the first reduction potentials (vs. Fc/Fc$^+$) for 1^+, 4^+, and 5^+ were recorded at −0.58 V, −0.82 V, and −0.71 V, respectively.
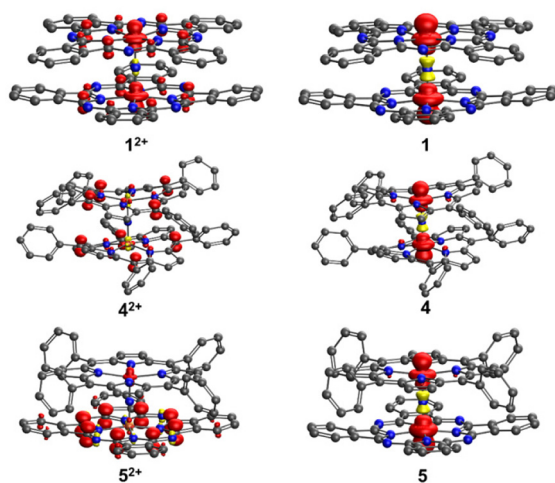

Fig. 7 Spin density in **1**, **4**, **5**, 1^{2+}, 4^{2+}, and 5^{2+}. In 1^+, 4^+, and 5^+, the spin density is zero everywhere. Hydrogen atoms are neglected for clarity.

The 1e$^-$-oxidation of 4^+, 1^+, and 5^+ induced negligible changes in the iron–ligand bond distances, suggesting that the oxidation mainly occurred within the macrocycles. Indeed, the spin density of μN in 4^{2+}, 1^{2+}, and 5^{2+} (Fig. 7) was negligible. For 1^{2+} and 4^{2+}, we observed that both macrocycles exhibited very similar densities, indicating that both complexes were partly oxidized. Conversely, in the case of 5^{2+}, the spin population of P was only 0.122, whereas the spin population of Pc was up to 0.8. This unambiguously pointed towards the phthalocyanine ring being the primary site of oxidation. The relatively higher tendency of phthalocyanine to be oxidized could be attributed to its longer conjugation length compared to that of porphyrin. The oxidation $\Delta G_{ox} = G_{X^{2+}} - G_{X^+}$ was also calculated. The oxidation energy of 1^+ was 5.6 eV, whereas for 4^+ and 5^+ very similar oxidation energies were observed (around 5.8 eV). These findings are consistent with the cyclic voltammetry data, according to which the first oxidation potentials (vs. Fc/Fc$^+$) for 1^+, 4^+, and 5^+ were found at −0.19 V, 0.55 V, and 0.53 V, respectively.

Further calculations were conducted to determine the reduction energy of the high-valent iron oxo species [$\mathbf{1}$=$\mathbf{O}$], [$\mathbf{4}$=$\mathbf{O}$], and [$\mathbf{5}$=$\mathbf{O}$] in water. As a result, we found the reduction free energies of [$\mathbf{1}$=$\mathbf{O}$], [$\mathbf{4}$=$\mathbf{O}$], and [$\mathbf{5}$=$\mathbf{O}$] to be very similar (around 4.6 eV). Moreover, it was found that catalytic CH$_4$ and CH$_3$CH$_3$ oxidation reactions via [$\mathbf{1}$=$\mathbf{O}$] in an acidic aqueous solution could not be quenched by addition of an excess Na$_2$SO$_3$, reducing reagent, and radical scavenger (entry 14 in Table S2,† (vide infra)),[36] whereas oxidation reactions via $^\bullet$OH could be significantly quenched under these conditions. It can be assumed that the oxidation reactions by [$\mathbf{4}$=$\mathbf{O}$] and [$\mathbf{5}$=$\mathbf{O}$] are less likely to be quenched by addition of Na$_2$SO$_3$.

CH$_4$ and CH$_3$CH$_3$ oxidation activity

In order to investigate the catalytic CH$_4$ and CH$_3$CH$_3$ oxidation activities of $1^+\cdot I^-$, $4^+\cdot I_3^-$, and $5^+\cdot I_3^-$ in an aqueous solution, we prepared silica gel supported catalysts ($1^+\cdot I^-$/SiO$_2$, $4^+\cdot I_3^-$/SiO$_2$, and $5^+\cdot I_3^-$/SiO$_2$) since these complexes are not soluble in aqueous solutions. The CH$_4$ and CH$_3$CH$_3$ oxidation reactions were performed in an acidic aqueous solution containing 57 μM of the catalyst molecule, 189 mM H$_2$O$_2$, and 51 mM trifluoroacetic acid (TFA) at 60 °C for 24 h under a CH$_4$ (or CH$_3$CH$_3$) atmosphere of 1.0 MPa.[15–17,22,24,25] After completion of the oxidation reaction, the oxidized products (MeOH, HCHO, and HCOOH for the CH$_4$ oxidation, and EtOH, CH$_3$CHO, AcOH, and HCOOH for the CH$_3$CH$_3$ oxidation) were quantified by GC-MS analysis, as summarized in Tables S1 and S2.†

To appropriately evaluate the catalytic CH$_4$ oxidation activity, the effective total turnover number (TTN$_{eff}$) was defined according to eqn (i) and (ii) for the CH$_4$ oxidation, and eqn (iii) and (iv) for the CH$_3$CH$_3$ oxidation, based on the idea that both CH$_4$ and CH$_3$CH$_3$ can be oxidized in a stepwise manner and summarized in Tables S1, S2† and Fig. 8.[15–17,22,24,25] We assumed that the small amount of oxidized products observed in the absence of CH$_4$ or CH$_3$CH$_3$ (under a N$_2$ atmosphere) could mainly originate from the
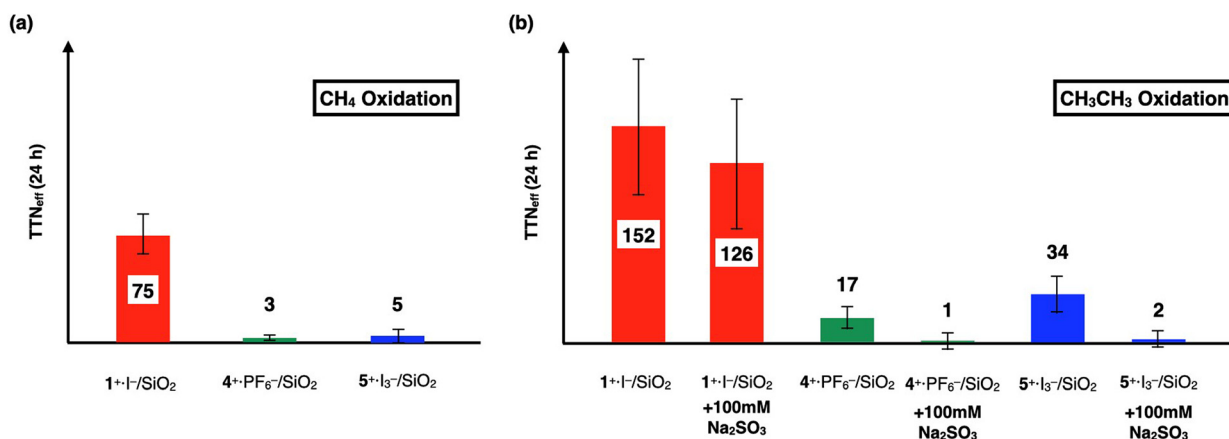
Fig. 8 (a) Comparison of TTN_{eff} for CH_4 oxidation for 24 h by $1^+ \cdot I^-$, $4^+ \cdot I_3^-$, and $5^+ \cdot I_3^-$. (b) Comparison of TTN_{eff} for CH_3CH_3 oxidation for 24 h by $1^+ \cdot I^-$, $4^+ \cdot I_3^-$, and $5^+ \cdot I_3^-$. Reactions were performed by using a silica gel-supported catalyst (30 mg, containing 57 μM of the catalyst molecule) in an aqueous solution (3.0 mL) containing H_2O_2 (189 mM) and TFA (51 mM) at 60 °C for 24 h under a CH_4, CH_3CH_3, or N_2 atmosphere (1.0 MPa). The amounts of each oxidized product in each oxidation reactions are summarized in Tables S1 and S2.†

adsorption of organic solvents on the silica-gel surface of the catalysts.

(CH_4 oxidation)

$$TTN_{eff}(CH_4) = TTN_{(CH_4)} - TTN_{(N_2)} \quad \text{(i)}$$

$$\begin{aligned} TTN(CH_4) \text{ or } TTN(N_2) \\ = (C_{MeOH} + 2 \times C_{HCHO} + 3 \times C_{HCOOH})/C_{Cat}, \end{aligned} \quad \text{(ii)}$$

(CH_3CH_3 oxidation)

$$TTN_{eff}(CH_3CH_3) = TTN_{(CH_3CH_3)} - TTN_{(N_2)} \quad \text{(iii)}$$

$$\begin{aligned} TTN(CH_3CH_3) \text{ or } TTN(N_2) = \\ (C_{EtOH} + 2 \times C_{HCHO} + 3 \times C_{AcOH} + 3 \times C_{HCOOH})/C_{Cat}, \end{aligned} \quad \text{(iv)}$$

We previously demonstrated that monocationic μ-nitrido-bridged iron phthalocyanine dimer $1^+ \cdot I^-$ acts as a CH_4 oxidation catalyst under similar reaction conditions.[16] Specifically, it was confirmed that both CH_4 and CH_3CH_3 were oxidized by $1^+ \cdot I^-/SiO_2$, as shown in Tables S1, S2,† and Fig. 8. Since the CH_3CH_3 oxidation reaction by $1^+ \cdot I^-/SiO_2$ was not significantly quenched in the presence of an excess amount of Na_2SO_3, a radical scavenger that could quench $^\bullet OH$ (entry 14 in Table S2,† and Fig. 8b),[36] and the color of $1^+ \cdot I^-/SiO_2$ was not apparently bleached after 24 h oxidation (Fig. S6†), the oxidation reactions promoted by $1^+ \cdot I^-/SiO_2$ were assumed to proceed through the formation of a high-valent iron-oxo species ($1=O$) rather than a Fenton-type reaction via $^\bullet OH$. Time dependencies of the TTN_{eff}s of CH_3CH_3 oxidations by the three catalysts are summarized in Table S2 and Fig. S5.† TTN_{eff}s seemed to be increased especially after 24 h for all of the catalysts, implying that decomposed catalysts showed Fenton-type oxidation, which can also be confirmed by the fact that the amounts of HCOOH were apparently increased at 48 h even in the absence of CH_3CH_3. We found it difficult to reuse these silica gel-supported catalysts for the catalytic oxidation

reactions because the silica gel supports became pulverized and some of the catalysts were detached and aggregated after long time stirring.

In contrast, both $4^+ \cdot I_3^-/SiO_2$ and $5^+ \cdot I_3^-/SiO_2$ did not show apparent CH_4 oxidation activities under these reaction conditions (entry 3 and 5 in Table S1,† and Fig. 8a). Although $4^+ \cdot I_3^-/SiO_2$ and $5^+ \cdot I_3^-/SiO_2$ showed CH_3CH_3 oxidation activities, as shown in entries 16 and 19 in Table S2,† and Fig. 8b, their catalytic CH_3CH_3 oxidation activities were significantly lower than that of $1^+ \cdot I^-/SiO_2$. Moreover, it was confirmed that the catalytic CH_3CH_3 oxidation activities of $4^+ \cdot I_3^-/SiO_2$ and $5^+ \cdot I_3^-/SiO_2$ could be apparently quenched in the presence of an excess amount of Na_2SO_3 (entries 17 and 20 in Table S2,† and Fig. 8b).

It should also be noted that both $4^+ \cdot I_3^-/SiO_2$ and $5^+ \cdot I_3^-/SiO_2$ did not show apparent color bleaching even after 24 h oxidation under these reaction conditions (Fig. S6†), indicating that the continuous occurrence of Fenton-type reactions is less probable. This is in clear contrast with the observation that monocationic μ-nitrido-bridged iron porphycene dimer $2^+ \cdot I_3^-$ showed complete bleaching under the same reaction conditions, which was elucidated by the instability of the high-valent iron-oxo species, as reported in our previous study.[24]

Considering that the results of the ESI-TOF MS experiments for $4^+ \cdot I_3^-$ and $5^+ \cdot I_3^-$ in the presence of H_2O_2 indicated the generation of high-valent iron-oxo species ($4=O$ and $5=O$), it seemed that the high-valent iron-oxo species of 4^+ and 5^+ were actually generated as in the case of 1 and 1^+. In addition, the majority of the CH_3CH_3 (or CH_4) oxidation reactions using $4^+ \cdot I_3^-/SiO_2$ and $5^+ \cdot I_3^-/SiO_2$ might be attributed to $^\bullet OH$, which could be catalytically generated from the small amount of the decomposed products of 4^+ and 5^+, since it was significantly quenched upon addition of Na_2SO_3 although the DFT calculations suggested that $4=O$ and $5=O$ could have similar reduction potential as $1=O$.

Therefore, the results of the CH_4 and CH_3CH_3 oxidation reactions in the presence of $4^+ \cdot I_3^-/SiO_2$ and $5^+ \cdot I_3^-/SiO_2$ at 24 h

(Fig. 8) implied that the catalytic alkane oxidation ability of **4**=**O** and **5**=**O** generated under these reaction conditions appeared to be much lower than that of **1**=**O**. Considering the differences in the crystal structures of the Fe–N=Fe moieties in **1**[+], **4**[+], and **5**[+] were not significant, the difference in catalytic activities could originate from that in the electronic structures of porphyrin and phthalocyanine, as indicated by the cyclic voltammetric studies of **1**[+], **4**[+], and **5**[+]. Notably, the 1e⁻-oxidation of **1**[+] corresponding to the 1e⁻-oxidation of the porphyrinoid ring occurred at a much lower potential (−0.19 V) than those of **4**[+] (0.55 V) and **5**[+] (0.53 V) could imply that the phthalocyanine moiety of **1**[+] possessed a more electron-rich character than those of the phthalocyanine moiety of **4**[+] and the porphyrin moiety of **5**[+].

The proposed reaction mechanism and possible elucidation of the contribution of the electron-rich character of the phthalocyanine moiety to the high CH₄ oxidation activity of **1**[+]·I⁻ are summarized in Fig. 9. The reactive intermediate is considered to be the *in situ* generated **1**=**O** species.[11] In general, the CH₄ oxidation by high-valent iron oxo species proceeds *via* a proton-coupled electron transfer (PCET) mechanism, in which the proton and electron abstraction from CH₄ occur in a concerted manner.[10] It can be expected that the electron-rich character of the phthalocyanine ring could increase the basicity of the oxo species. Another possibility is that the heterolytic cleavage of the O–O bonding of hydroperoxo species to give the high-valent iron-oxo species (**1**=**O**) is facilitated by the electron-rich phthalocyanine moiety, as in the case with a push effect.[16,37,38] Exact determination of rate constants for the reactions by **4**[+] and **5**[+] were difficult because they apparently include Fenton-type reaction. On the other hand, although the reaction by **1**[+]·I⁻/SiO₂ is considered to be proceeded mainly *via* high-valent iron-oxo species, determination of the production rate of **1**=**O** was also difficult due to

both of the catalase reaction, which competed with the alkane oxidation by converting H₂O₂ into O₂, and the silica-gel support, which readily adsorbed the organic dyes added in the solution in order to determine the production rate of the oxo species.

Sorokin *et al.* reported that **4**/SiO₂ exhibited an apparent catalytic CH₄ oxidation activity to give HCOOH as a major product in an aqueous solution by using *m*CPBA as an oxidant instead of H₂O₂.[18] Considering that both **4** and **4**[+] can generate the same high-valent iron-oxo species **4**=**O** upon reacting with H₂O₂, it is unlikely that the difference in the oxidation state (**4** and **4**[+]) significantly affected the catalytic activity. Actually, in the case of a μ-nitrido-bridged iron phthalocyanine dimer, **1** and **1**[+] showed a similar catalytic activity in an acidic aqueous solution containing H₂O₂.[17] Therefore, we concluded that the reason why **4**[+] did not show apparent CH₄ oxidation ability could mainly be due to the different oxidant (*m*CPBA and H₂O₂). It is probable that the coordination of the *m*-chlorobenzoic acid anion onto the other side of the iron center of the high-valent iron-oxo species, as suggested by the DFT calculations conducted by de Visser *et al.*, could have changed the electronic character and reactivity of the high-valent iron-oxo species of **4**[+].[19]

Conclusions

In this study, we synthesized a monocationic μ-nitrido-bridged porphyrin heterodimer (**4**[+]) along with a monocationic μ-nitrido-bridged heterodimer of iron phthalocyanine and iron porphyrin (**5**[+]) and compared their electrochemical and spectroscopic properties with those of a monocationic μ-nitrido-bridged iron phthalocyanine homodimer (**1**[+]), which showed potent catalytic CH₄ oxidation activity in an acidic aqueous solution in the presence of H₂O₂. Single-crystal X-ray structural analysis demonstrated that the Fe–N=Fe core structures of **4**[+]·I₃⁻ and **5**[+]·I₃⁻ were similar to that of **1**[+]·I. We also confirmed that the high-valent iron-oxo species of **4**[+] and **5**[+] were actually observed by ESI-TOF MS spectroscopy in the presence of H₂O₂. It was demonstrated that the catalytic CH₄ and CH₃CH₃ oxidation activities of **4**[+]·I₃⁻ and **5**[+]·I₃⁻ were significantly lower than that of **1**[+]·I⁻ in an acidic aqueous solution at 60 °C in the presence of an excess of H₂O₂. These results clearly indicated that the difference in the porphyrinoid ring of the monocationic μ-nitrido-bridged iron porphyrinoid dimer strongly affected the electronic structure and reactivity of the high-valent iron-oxo species generated from monocationic μ-nitrido-bridged iron porphyrinoid dimers.

Fig. 9 Proposed reaction mechanism and possible elucidation for the contribution of electron-donation by phthalocyanine ring to the high methane oxidation activity of **1**[+].

Experimental

General

All reagents and solvents were purchased at the highest commercial quality available and used without further purification, unless otherwise stated. ¹H NMR spectra were recorded on a
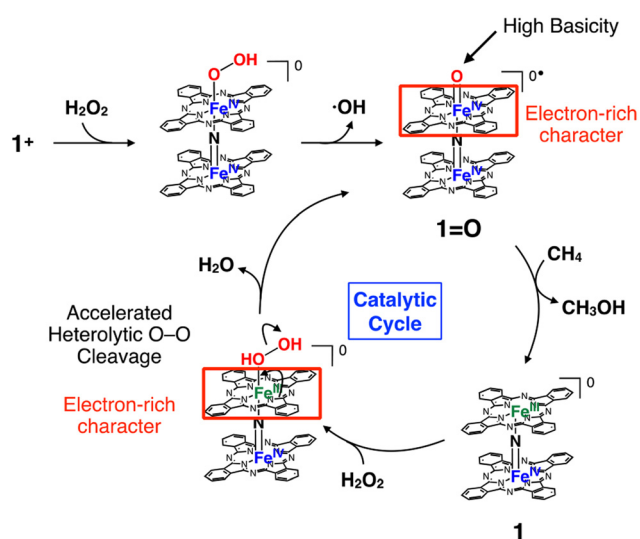
JEOL JNM-ECS400 (400 MHz for ^{1}H) spectrometer at a constant temperature of 298 K. Elemental analysis was performed on a Yanaco MT-6 analyzer. The absorption spectrum was recorded with a Hitachi U-4100 spectrophotometer in pyridine solutions at 20 ± 0.1 °C in 1.0 cm quartz cells. MALDI-TOF MS was performed on Bruker Daltonics ultrafleXtreme using α-CHCA as a matrix. MALDI-TOF MS was performed on Bruker Daltonics compact.

Synthesis of $4^+ \cdot I_3^-$

A mixture of **6** (201 mg, 0.29 mmol), NaN_3 (212 mg, 3.3 mmol) and 1-chloronaphthalene (5.0 mL) was heated under air at 280 °C for 2 h. After cooling to room temperature, the reaction mixture was diluted with CH_2Cl_2 (200 mL). The solution was washed with H_2O (100 mL × 2) and brine (100 mL × 2) then evaporated to give a reddish-brown crude solid. The crude product was dissolved in CH_2Cl_2 (150 mL). After iodine (552 mg, 4.3 mmol as I) was added, the resulting solution was stirred for 2 h at room temperature, followed by evaporation of the volatile compounds. The residue was washed with Et_2O (300 mL) to remove the remaining iodine, and then, dried under reduced pressure to give reddish brown solid. The crude was purified by silica gel column chromatography (⌀ 4.5 cm × 16.0 cm, CH_2Cl_2, then CH_2Cl_2/MeOH = 20/1) and recrystallization of CH_2Cl_2/Et_2O to yield $4^+ \cdot I_3^-$ as a reddish brown solid (176 mg, 71%). ^{1}H-NMR (400 MHz, pyridine-d_5/TMS): $\delta = 9.08$ (d, $J = 7.6$ Hz, 8H), 8.81 (s, 16H), 8.21 (t, $J = 7.4$ Hz, 8H), 8.00 (t, $J = 7.6$ Hz, 8H), 7.67 (t, $J = 7.6$ Hz, 8H), 7.37 (d, $J = 7.6$ Hz, 8H). MALDI-TOF MS: $m/z = 1350.34$: calcd for $C_{88}H_{56}Fe_2N_9$ ([M]$^+$) found: 1350.35. Anal. calcd for $C_{88}H_{56}Fe_2I_3N_9O_5$ ($4^+ \cdot I_3^-$): C; 61.03, H; 3.26, N; 7.28, found: C; 61.15, H; 3.31, N; 6.95 (0.33% error).

Synthesis of $4^+ \cdot PF_6^-$

$4^+ \cdot I_3^-$ (50 mg, 29 μmol) was dissolved in 10 mL of 1 : 1 (v/v) mixture of pyridine and CH_3CN. After KPF_6 (541 mg, 2.9 mmol) in 1 : 1 (v/v) mixture of pyridine and CH_3CN (10 mL) was added to the solution, H_2O (80 mL) was added. The resulting precipitate was collected by centrifugation, followed by decantation to yield reddish brown solid (49.7 mg). The crude product was further purified by recrystallization from CH_2Cl_2/Et_2O to give the desired product $4^+ \cdot PF_6^-$ as a reddish brown solid (41 mg, 27 μmol, 94%). ^{1}H-NMR (400 MHz, pyridine-d_5/TMS): $\delta = 9.08$ (d, $J = 8.0$ Hz, 8H), 8.82 (s, 16H), 8.21 (t, $J = 7.6$ Hz, 8H), 8.00 (t, $J = 7.4$ Hz, 8H), 7.66 (t, $J = 8.0$ Hz, 8H), 7.36 (d, $J = 8.4$ Hz, 8H). MALDI-TOF MS: $m/z = 1350.34$: calcd for $C_{88}H_{56}Fe_2N_9$ ([M]$^+$) found: 1350.35. Anal. calcd for $C_{76}H_{44}F_6Fe_2N_{13}P$ ($4^+ \cdot PF_6^- \cdot 2Py \cdot 2CH_2Cl_2$): C; 65.84, H; 3.87, N; 8.45, found: C; 66.18, H; 3.55, N; 8.49 (0.34% error).

Synthesis of $5^+ \cdot I_3^-$

A mixture of **6** (105 mg, 0.15 mmol), **7** (85 mg, 0.15 mmol), NaN_3 (201 mg, 3.1 mmol) and 1-chloronaphtalene (5.0 mL) was heated under air at 280 °C for 2 h. After cooling to room temperature, the reaction mixture was diluted with hexane (400 mL), the precipitate was collected by suction filtration,

washed with H_2O (300 mL), dried under vacuum to give blackish green crude solid (234 mg). The crude product was dissolved in pyridine (200 mL). After iodine (215 mg, 0.85 mmol as I) was added, the resulting solution was stirred for 2 h at room temperature, followed by evaporation of the volatile compounds. The residue was washed with Et_2O (300 mL) to remove the remaining iodine, and then, dried under reduced pressure to give dark green solid. The crude was purified by silica gel column chromatography (⌀ 4.5 cm × 16.0 cm, CH_2Cl_2/AcOEt = 1/1, then CH_2Cl_2/AcOEt/MeOH = 10/10/1) and recrystallization of CH_2Cl_2/Et_2O to yield $5^+ \cdot I_3^-$ as a dark green solid (174 mg, 71%). ^{1}H-NMR (400 MHz, pyridine-d_5/TMS): $\delta = 11.00$ (d, $J = 8.0$ Hz, 4H), 9.82 (dd, $J = 5.6$, 3.2 Hz, 8H), 8.83 (t, $J = 7.8$ Hz, 4H), 8.38 (dd, $J = 5.6$, 2.8 Hz, 8H), 8.29 (s, 8H), 8.07 (t, $J = 8.0$ Hz, 4H), 7.53–7.58 (m, 4H), 7.21–7.25 (m, 4H). MALDI-TOF MS: $m/z = 1250.25$: calcd for $C_{76}H_{44}Fe_2N_{13}$ ([M]$^+$) found: 1250.39. Anal. calcd for $C_{90}H_{64}Fe_2I_3N_{15}O$ ($5^+ \cdot I_3^- \cdot 2Py \cdot Et_2O$): C; 57.99, H; 3.46, N; 11.27, found: C; 57.83, H; 3.11, N; 11.15 (0.35% error).

Synthesis of $5^+ \cdot PF_6^-$

$5^+ \cdot I_3^-$ (60 mg, 37 μmol) was dissolved in 10 mL of 1 : 1 (v/v) mixture of pyridine and CH_3CN. After KPF_6 (704 mg, 3.8 mmol) in 1 : 1 (v/v) mixture of pyridine and CH_3CN (10 mL) was added to the solution, H_2O (80 mL) was added. The resulting precipitate was collected by centrifugation, followed by decantation to yield dark green solid (80 mg). The crude product was further purified by recrystallization from CH_2Cl_2/Et_2O to give the desired product $5^+ \cdot PF_6^-$ as a dark green solid (48 mg, 34 μmol, 93%). ^{1}H-NMR (400 MHz, pyridine-d_5/TMS): $\delta = 11.00$ (d, $J = 8.4$ Hz, 4H), 9.82 (dd, $J = 5.6$, 3.0 Hz, 8H), 8.83 (t, $J = 8.0$ Hz, 4H), 8.38 (dd, $J = 5.4$, 2.2 Hz, 8H), 8.29 (s, 8H), 8.07 (t, $J = 7.8$ Hz, 4H), 7.5–7.58 (m, 4H), 7.21–7.28 (m, 4H). MALDI-TOF MS: $m/z = 1250.25$: calcd for $C_{76}H_{44}Fe_2N_{13}$ ([M]$^+$) found: 1250.39. Anal. calcd for $C_{77}H_{46}Cl_2F_6Fe_2N_{13}P$ ($5^+ \cdot PF_6^- \cdot CH_2Cl_2$): C; 62.45, H; 3.13, N; 12.30, found: C; 62.24, H; 3.02, N; 12.50 (0.21% error).

Single-crystal X-ray structural analyses of $4^+ \cdot I_3^-$ and $5^+ \cdot I_3^-$

Crystal suitable for single-crystal X-ray structural analysis was obtained by slow evaporation of solvent from a $4^+ \cdot I_3^-$ (or $5^+ \cdot I_3^-$) solution in a 1 : 50 (v/v) mixture of pyridine and $CHCl_3$. Single-crystal X-ray diffraction measurements were performed using a Rigaku X-ray diffractometer equipped with a molybdenium MicroMax-007 and Saturn 70 CCD detector. The measurement was performed at 123 K. The structure was solved *via* the direct method (SHELXT) and refined *via* full-matrix least-squares on F_2 (SHELX-2018) using Olex2-1.3 program All non-hydrogen atoms were refined anisotropically. Geometrical restraints were applied: DFIX, SADI, DELU, ISOR, and OMIT. The crystal datas are as follows:

$4^+ \cdot I_3^-$: Formula $C_{360}H_{232}Cl_{48}Fe_8I_{12}N_{60}$, FW = 9069.594, crystal size 0.04 × 0.16 × 0.18 mm^3, triclinic, space group $P\bar{1}$, $a = 15.1304(17)$ Å, $b = 20.032(2)$ Å, $c = 29.169(3)$ Å, $\alpha = 90°$, $\beta = 92.653(7)°$, $\gamma = 90°$, $V = 8831.5(18)$ Å^3, $Z = 1$, $R_1 = 0.0941(35\,119)$ ($I > 2(I)$), $wR_2 = 0.2427(40\,518)$ (all), GOF = 1.031. CCDC identi-

fication code 2242976.† All the checkCIF Level-B alerts are due to the low crystal quality.

$5^+ \cdot I_3^-$: Formula $C_{388}H_{260}Cl_{48}Fe_8I_{12}N_{40}$, FW = 9153.994, crystal size $0.10 \times 0.10 \times 0.10$ mm^3, triclinic, space group $P\bar{1}$, a = 20.2412(6) Å, b = 15.9489(5) Å, c = 27.7869(8) Å, α = 90°, β = 90°, γ = 90°, V = 8970.3(5) Å^3, Z = 1, R_1 = 0.0382(22 741) ($I > 2$ (I)), wR_2 = 0.1515(25 785) (all), GOF = 1.300. CCDC identification code 2242975.† All the checkCIF Level-B alerts are due to the low crystal quality.

Cyclic voltammogram of $4^+ \cdot PF_6^-$, $5^+ \cdot PF_6^-$

Cyclic voltammograms were measured with a BAS Electrochemical Analyzer Model 750Ds at room temperature in pyridine solutions containing 100 mM TBAPF$_6$ in a standard one-component cell under an N$_2$ atmosphere equipped with a 3 mm-O.D. glassy carbon disk working electrode, platinum wire counter electrode, and Ag/AgCl reference electrode. All solutions were deoxygenated by N$_2$ bubbling for at least 20 min. Obtained $E^{\circ\prime}$ vs. Ag/AgCl were converted to those vs. Fc/Fc$^+$ based on measured redox potential of ferrocene. Tetrabutylammonium hexafluorophosphate (TBA$^+$PF$_6^-$) was recrystallized from 95% EtOH and dried under vacuum overnight at 100 °C.

ESI-TOF MS measurement of $5^+ \cdot I_3^-$ in CH$_3$CN in the presence of H$_2$O$_2$

To a solution of $5^+ \cdot I_3^-$ in CH$_3$CN (2.0 mL, 1.0 μM) was added 35% aqueous H$_2$O$_2$ (0.1 mL, 1.16 mmol). After addition, the resulting mixture was subjected to ESI-TOF MS measurement immediately.

DFT calculation

DFT calculations of **1**, **4**, and **5** were performed with the BP86-D3(BJ)/def2-TZVP level of theory implemented in the Turbomole software package.[39–42] This level was chosen based on our previous study as well as the works of Sorokin et al.[11] To ensure the validity of the optimized structures and to acquire Gibbs free energies,[43] frequency calculations were carried out. On top of the optimized structures, single-point calculations combined with the COSMO model were done to account for the solvent effect (pyridine with a dielectric constant of 12.5).[44] Wiberg bond order indices in the natural atomic orbital (NAO) basis were obtained at the same level of theory, using the Gaussian 16 and Multiwfn packages.[45,46]

The structures of the oxo complexes were obtained at the B3LYP-D3(BJ)/def2-TZVP level of theory. For the neutral species, only the doublet state $Fe^{IV}Fe^{IV}O(P^{\bullet+})$ was considered. For the anion species, the open-shell singlet state $Fe^{IV}Fe^{IV}O(P)$ was calculated. To account for the water solvent, CPCM solvation model was employed.[47] The calculations were done with the Orca 5.0 package.[48]

CH$_4$ or CH$_3$CH$_3$ oxidation reactions

Heterogeneous CH$_4$ or CH$_3$CH$_3$ oxidation reaction was performed in a stainless-steel autoclave with a glass tube. A mixture containing the catalyst on SiO$_2$ (30 mg, 55 μM as

$4^+ \cdot I_3^-$, or $5^+ \cdot I_3^-$, or $1^+ \cdot I^-$), 35% aqueous H$_2$O$_2$ (50 μL, 189 mM), and TFA (12 μL, 51 mM) in H$_2$O (3.0 mL) was heated at 60 °C under 1.0 MPa of CH$_4$ (or CH$_3$CH$_3$, or N$_2$) atmosphere for 24 h with continuous stirring (900 rpm). After the autoclave was opened, the reaction mixture was filtrated through a disposable membrane filter (DISMIC-13CP, ADVANTEC). The filtrate was analyzed by GC-MS (system: Agilent 7890A equipped with JEOL JMS-T100GCV, detection: EI, column: Agilent DB-WAX UI, external standard: isovaleric acid (5 mM), temperature conditions: initial: 70 °C to 220 °C (10 °C min^{-1}) – hold (5 min)). The yields of CH$_3$OH, EtOH, CH$_3$CHO, AcOH and formic acid were determined based on the results of GC-MS. The yield of formaldehyde was examined using the method reported in our previous paper.[15–17,22,24,25]

Conflicts of interest

There are no conflicts to declare.

Acknowledgements

References

1 P. Schwach, X. Pan and X. Bao, *Chem. Rev.*, 2017, **117**, 8497–8520.

2 M. Ravi, M. Ranocchiari and J. A. van Bokhoven, *Angew. Chem., Int. Ed.*, 2017, **56**, 16464–16483.

3 C. E. Tinberg and S. J. Lippard, *Acc. Chem. Res.*, 2011, **44**(4), 280–288.

4 S. Sirajuddin and A. C. Rosenzweig, *Biochemistry*, 2015, **54**, 2283–2294.

5 V. C.-C. Wang, S. Maji, P. P.-Y. Chen, H. K. Lee, S. S.-F. Yu and S. I. Chan, *Chem. Rev.*, 2017, **117**, 8574–8621.

6 A. R. McDonald and L. Que Jr., *Coord. Chem. Rev.*, 2013, **257**, 414–428.

7 M. Guo, T. Corona, K. Ray and W. Nam, *ACS Cent. Sci.*, 2019, **5**, 13–28.

8 C. V. Sastri, J. Lee, K. Oh, Y. J. Lee, J. Lee, T. A. Jackson, K. Ray, H. Hirao, W. Shin, J. A. Halfen, J. Kim, L. Que Jr., S. Shaik and W. Nam, *Proc. Natl. Acad. Sci. U. S. A.*, 2007, **104**, 19181–19186.

9 Y. J. Jeong, Y. Kang, A.-R. Han, Y.-M. Lee, H. Kotani, S. Fukuzumi and W. Nam, *Angew. Chem.*, 2008, **120**, 7431–7434.

10 J. E. M. N. Klein and G. Knizia, *Angew. Chem., Int. Ed.*, 2018, **57**, 11913–11917.

11 P. Afanasiev and A. B. Sorokin, *Acc. Chem. Res.*, 2016, **49**, 583–593.

12 H. Fujisaki and T. Kojima, *Catal. Sci. Technol.*, 2023, **13**, 4270–4284.

13 A. B. Sorokin, E. V. Kudrik and D. Bouchu, *Chem. Commun.*, 2008, 2562–2564.

14 Ü. İşci, A. S. Faponle, P. Afanasiev, F. Albrieux, V. Briois, V. Ahsen, F. Dumoulin, A. B. Sorokin and S. P. de Visser, *Chem. Sci.*, 2015, **6**, 5063–5075.

15 Y. Yamada, K. Morita, N. Mihara, K. Igawa, K. Tomooka and K. Tanaka, *New J. Chem.*, 2019, **43**, 11477–11482.

16 Y. Yamada, J. Kura, Y. Toyoda and K. Tanaka, *Dalton Trans.*, 2021, **50**, 6718–6724.

17 Y. Yamada, K. Morita, T. Sugiura, Y. Toyoda, N. Mihara, M. Nagasaka, H. Takaya, K. Tanaka, T. Koitaya, N. Nakatani, H. Ariga-Miwa, S. Takakusagi, Y. Hitomi, T. Kudo, Y. Tsuji, K. Yoshizawa and K. Tanaka, *JACS Au*, 2023, **3**, 823–833.

18 E. V. Kudrik, P. Afanasiev, L. X. Alvarez, P. Dubourdeaux, M. Clémancey, J.-M. Latour, G. Blondin, D. Bouchu, F. Albrieux, S. E. Nefedov and A. B. Sorokin, *Nat. Chem.*, 2012, **4**, 1024–1029.

19 M. G. Quesne, D. Senthilnathan, D. Singh, D. Kumar, P. Maldivi, A. B. Sorokin and S. P. de Visser, *ACS Catal.*, 2016, **6**, 2230–2243.

20 E. V. Kudrik and A. B. Sorokin, *Chem. – Eur. J.*, 2008, **14**, 7123–7126.

21 L. X. Alvarez and A. B. Sorokin, *J. Organomet. Chem.*, 2015, **793**, 139–144.

22 N. Mihara, Y. Yamada, H. Takaya, Y. Kitagawa, K. Igawa, K. Tomooka, H. Fujii and K. Tanaka, *Chem. – Eur. J.*, 2019, **25**, 3369–3375.

23 Y. Yamada, C.-M. Teoh, Y. Toyoda and K. Tanaka, *New J. Chem.*, 2022, **46**, 955–958.

24 Y. Yamada, Y. Miwa, Y. Toyoda, T. Yamaguchi, S. Akine and K. Tanaka, *Dalton Trans.*, 2021, **50**, 16775–16781.

25 Y. Yamada, Y. Miwa, Y. Toyada, Q. M. Phung, K. Oyama and K. Tanaka, *Catal. Sci. Technol.*, 2023, **13**, 1725–1734.

26 D. A. Summerville and I. A. Cohen, *J. Am. Chem. Soc.*, 1976, **98**, 1747–1752.

27 C. Ercolani, M. Gardini, G. Pennesi, G. Rossi and U. Russo, *Inorg. Chem.*, 1988, **27**, 422–424.

28 D. R. English, D. N. Hendrickson and K. S. Suslick, *Inorg. Chem.*, 1985, **24**, 122–127.

29 Y. Yamada, T. Sugiura, K. Morita, H. Ariga-Miwa and K. Tanaka, *Inorg. Chim. Acta*, 2019, **489**, 160–163.

30 K. M. Kadish, R. K. Rhodes, L. A. Bottomley and H. M. Goff, *Inorg. Chem.*, 1981, **20**, 3195–3200.

31 L. A. Bottomley and B. B. Garrett, *Inorg. Chem.*, 1982, **21**, 1260–1263.

32 T. Shimizu, K. Wakamatsu, Y. Yamada, Y. Toyoda, S. Akine, K. Yoza and H. Yoshikawa, *ACS Appl. Mater. Interfaces*, 2021, **13**, 40612–40617.

33 T. Guchhait, S. Sasmal, F. S. T. Khan and S. P. Rath, *Coord. Chem. Rev.*, 2017, **337**, 112–144.

34 L. A. Bottomley, J.-N. Gorce, V. L. Goedken and C. Ercolani, *Inorg. Chem.*, 1985, **24**, 3733–3737.

35 A. Ghosh, E. Tangen, E. Gonzalez and L. Que Jr., *Angew. Chem.*, 2004, **116**, 852–856.

36 C. Hammond, M. M. Forde, M. H. Ab Rahim, A. Thetford, Q. He, R. L. Jenkins, N. Dimitratos, J. A. Lopez-Sanchez, N. F. Dummer, D. M. Murphy, A. F. Carley, S. H. Taylor, D. J. Willock, E. E. Stangland, J. Kang, H. Hagen, C. J. Kiely and G. J. Hutchings, *Angew. Chem., Int. Ed.*, 2012, **51**, 5129–5133.

37 K. Yamaguchi, Y. Watanabe and I. Morishima, *Inorg. Chem.*, 1992, **31**, 156–157.

38 Y. Watanabe, High-Valent Intermediates, in *The Porphyrin Handbook*, ed. K. M. Kadish, K. M. Smith and R. Guilard, Elsevier, 2003, vol. 4, ch. 30.

39 S. G. Balasubramani, G. P. Chen, S. Coriani, M. Diedenhofen, M. S. Frank, Y. J. Franzke, F. Furche, R. Grotjahn, M. E. Harding, C. Hättig, A. Hellweg, B. Helmich-Paris, C. Holzer, U. Huniar, M. Kaupp, A. Marefat Khah, S. Karbalaei Khani, T. Müller, F. Mack, B. D. Nguyen, S. M. Parker, E. Perlt, D. Rappoport, K. Reiter, S. Roy, M. Rückert, G. Schmitz, M. Sierka, E. Tapavicza, D. P. Tew, C. van Wüllen, V. K. Voora, F. Weigend, A. Wodyński and J. M. Yu, *J. Chem. Phys.*, 2020, **152**, 184107.

40 F. Weigend and R. Ahlrichs, *Phys. Chem. Chem. Phys.*, 2005, **7**, 3297–3305.

41 S. Grimme, *Wiley Interdiscip. Rev.: Comput. Mol. Sci.*, 2011, **1**, 211–228.

42 S. Grimme, S. Ehrlich and L. Goerigk, *J. Comput. Chem.*, 2011, **32**, 1456–1465.

43 S. Grimme, *Chem. – Eur. J.*, 2012, **18**, 9955–9964.

44 A. Klamt and G. Schüürmann, *J. Chem. Soc., Perkin Trans. 2*, 1993, 799–805.

45 M. J. Frisch, G. W. Trucks, H. B. Schlegel, G. E. Scuseria, M. A. Robb, J. R. Cheeseman, G. Scalmani, V. Barone, G. A. Petersson, H. Nakatsuji, X. Li, M. Caricato, A. V. Marenich, J. Bloino, B. G. Janesko, R. Gomperts, B. Mennucci, H. P. Hratchian, J. V. Ortiz, A. F. Izmaylov, J. L. Sonnenberg, D. Williams-Young, F. Ding, F. Lipparini, F. Egidi, J. Goings, B. Peng, A. Petrone, T. Henderson, D. Ranasinghe, V. G. Zakrzewski, J. Gao, N. Rega, G. Zheng, W. Liang, M. Hada, M. Ehara, K. Toyota, R. Fukuda, J. Hasegawa, M. Ishida, T. Nakajima, Y. Honda, O. Kitao, H. Nakai, T. Vreven, K. Throssell, J. A. Montgomery Jr., J. E. Peralta, F. Ogliaro, M. J. Bearpark, J. J. Heyd, E. N. Brothers, K. N. Kudin, V. N. Staroverov, T. A. Keith, R. Kobayashi, J. Normand, K. Raghavachari, A. P. Rendell, J. C. Burant, S. S. Iyengar, J. Tomasi, M. Cossi, J. M. Millam, M. Klene, C. Adamo, R. Cammi, J. W. Ochterski, R. L. Martin, K. Morokuma, O. Farkas,

J. B. Foresman and D. J. Fox, *Gaussian 16, Revision C.01*, Gaussian, Inc., Wallingford CT, 2016.

46 T. Lu and F. Chen, *J. Comput. Chem.*, 2012, **33**, 580–592.

47 V. Barone and M. Cossi, *J. Phys. Chem. A*, 1998, **102**, 1995–2001.

48 F. Neese, *Wiley Interdiscip. Rev.: Comput. Mol. Sci.*, 2022, **12**, e1606.